Wright State University

CORE Scholar

Mathematics and Statistics Faculty Publications

Mathematics and Statistics

8-5-2005

Investigation of Laser Beam Induced Current Techniques for Heterojunction Photodiode Characterization

Weifu Fang
Wright State University - Main Campus, weifu.fang@wright.edu

David A. Redfern

Kazufumi Ito

G. Bahir

Charles A. Musca

See next page for additional authors

Follow this and additional works at: https://corescholar.libraries.wright.edu/math

Repository Citation

Fang, W., Redfern, D. A., Ito, K., Bahir, G., Musca, C. A., Dell, J. M., & Faraone, L. (2005). Investigation of Laser Beam Induced Current Techniques for Heterojunction Photodiode Characterization. *Journal of Applied Physics, 98* (3), 34501.
https://corescholar.libraries.wright.edu/math/427

This Article is brought to you for free and open access by the Mathematics and Statistics department at CORE Scholar. It has been accepted for inclusion in Mathematics and Statistics Faculty Publications by an authorized administrator of CORE Scholar. For more information, please contact library-corescholar@wright.edu.

Authors
Weifu Fang, David A. Redfern, Kazufumi Ito, G. Bahir, Charles A. Musca, John M. Dell, and Lorenzo Faraone

This article is available at CORE Scholar: https://corescholar.libraries.wright.edu/math/427

Journal of Applied Physics

Investigation of laser beam-induced current techniques for heterojunction photodiode characterization

Cite as: J. Appl. Phys. **98**, 034501 (2005); https://doi.org/10.1063/1.1993754
Submitted: 29 March 2005 • Accepted: 10 June 2005 • Published Online: 05 August 2005

D. A. Redfern, W. Fang, K. Ito, et al.

ARTICLES YOU MAY BE INTERESTED IN

The role of localized junction leakage in the temperature-dependent laser-beam-induced current spectra for HgCdTe infrared focal plane array photodiodes
Journal of Applied Physics **114**, 173107 (2013); https://doi.org/10.1063/1.4829452

Temperature-sensitive junction transformations for mid-wavelength HgCdTe photovoltaic infrared detector arrays by laser beam induced current microscope
Applied Physics Letters **105**, 191106 (2014); https://doi.org/10.1063/1.4901529

Novel signal inversion of laser beam induced current for femtosecond-laser-drilling-induced junction on vacancy-doped p-type HgCdTe
Journal of Applied Physics **115**, 204506 (2014); https://doi.org/10.1063/1.4879316

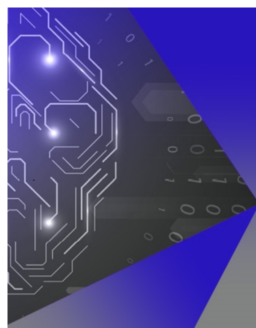

APL Machine Learning
Machine Learning for Applied Physics
Applied Physics for Machine Learning
First Articles Now Online!

AIP Publishing

© 2005 American Institute of Physics.

HTML ABSTRACT + LINKS

Investigation of laser beam-induced current techniques for heterojunction photodiode characterization

D. A. Redfern[a)]
School of Electrical, Electronic and Computer Engineering, The University of Western Australia, 35 Stirling Highway, Crawley 6009, Australia

W. Fang
Department of Mathematics, West Virginia University, Morgantown, West Virginia 26506

K. Ito
Department of Mathematics, North Carolina State University, Raleigh, North Carolina 27695

G. Bahir
Department of Electrical Engineering, Technion-Israel Institute of Technology, Haifa 32000, Israel

C. A. Musca, J. M. Dell, and L. Faraone[b)]
School of Electrical, Electronic and Computer Engineering, The University of Western Australia, 35 Stirling Highway, Crawley 6009, Australia

(Received 29 March 2005; accepted 10 June 2005; published online 5 August 2005)

A reduced model is developed that has significant advantages over the full drift-diffusion model for the simulation of laser beam-induced current (LBIC) signals in the presence of heterojunctions. The model determines the contribution to the LBIC signal that would occur from photogeneration at any position within the semiconductor, and is particularly useful for heterostructures where judicious choice of illumination wavelength can result in photogeneration at different depths within the device structure. The reduced model is used to examine the basic features of LBIC as applied to two types of planar *P-n* HgCdTe heterojunction photodiode structures. In particular, the question of correctly identifying erroneous device structures formed during the fabrication process is addressed, and experimental measurements are presented to support the simulation results. © *2005 American Institute of Physics*. [DOI: 10.1063/1.1993754]

I. INTRODUCTION

Photodiodes fabricated from HgCdTe *P*-on-*n* heterojunctions are finding increasing use in commercial applications involving the detection of infrared radiation due to their significantly higher performance in comparison to *p-n* homojunction photodiodes.[1,2] In particular, they have the potential for a much higher R_0A than industry-standard *n*-on-*p* homojunctions for several reasons. Firstly, the doping of the relatively thick *n*-type epitaxial layer in a *P*-on-*n* structure can be controlled to lower levels by extrinsic techniques during the growth process in comparison to what is achievable for the *p*-type doping of the thick *p*-type epitaxial layer required for *n*-on-*p* homojunctions. This reduced *n*-type doping is associated with longer diffusion lengths and correspondingly higher values of junction dynamic resistance at diffusion limited temperatures. Additionally, the wider band-gap *P*-type layer has a much lower intrinsic carrier concentration, and hence a reduced minority electron diffusion current contribution to the total dark current in comparison to the homojunction equivalent.

There are two dominant architectures for planar HgCdTe *P*-on-*n* heterojunction photodiodes described in the literature, which are depicted in Fig. 1. Note that the convention used in this paper is that n^+ represents a higher doping level than n, and N and P represent wider band-gap materials than n and p, respectively. Workers from Rockwell[3–5] have used an *N*-on-*n* as-grown-layered structure, and ion implantation

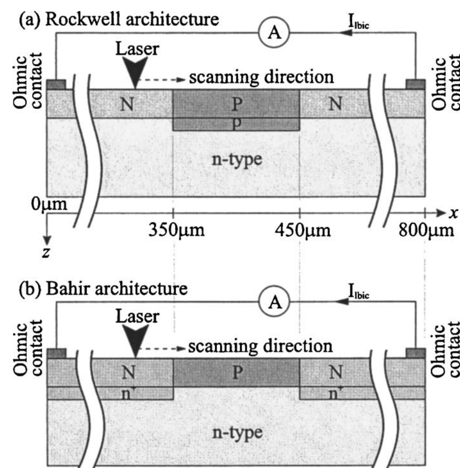

FIG. 1. The LBIC set-up on the two main architectures used for planar *P*-on-*n* heterojunction photodiodes, of (a) Rockwell (Refs. 3–5), and (b) of Bahir (Refs. 6 and 7). The convention used in this paper is that n^+ represents a higher doping level than n, and N and P represent wider band-gap materials than n and p, respectively. For the two-dimensional simulations in this paper the *P*-type region extends from the 350 to the 450 μm position and the ohmic contacts are placed on the top surface of the 800 μm long structure.

[a)]Present address: Institute of Industrial Sciences, The University of Tokyo 4-6-1 Komaba, Meguro-ku, Tokyo 153-8505, Japan; electronic mail: redfern@iis.u-tokyo.ac.jp

[b)]FAX: +61 8 6488 1095; electronic mail: faraone@ee.uwa.edu.au

 © 2005 American Institute of Physics

of acceptor dopants to form P-on-n diodes. In this configuration the depth placement of the junction is critical due to the fact that if the acceptor-doped region does not reach the narrow band-gap n-type detecting material the device performance will be severely compromised. Alternatively, if the junction is too deep the device will behave essentially as a p-on-n homojunction, and the advantages of the wider band-gap P-type material in the heterojunction cannot be taken advantage of.

The second P-on-n heterojunction architecture is fabricated by starting with an as-grown P-on-n material and isolating the individual diodes by using a gridlike pattern of donor doping. This architecture was described by Bahir[6] but has also been adopted more recently by other workers.[2,7–9] In this device architecture the relative positions of the heterojunction and metallurgical junctions are determined by the initial growth process. The isolating donor dopant is required to extend to a depth that is sufficient to reach the underlying narrow band-gap n-type material in order for the individual P-on-n devices to be defined, otherwise there is no other requirement for a specific depth to be achieved. It is the determination of the depth of the implanted acceptor doping in the Rockwell architecture, or the isolating donor doping in the Bahir architecture, in relation to the heterointerface that is the primary focus of this paper.

Laser beam-induced current (LBIC) is a semiconductor characterization technique that has been used in a qualitative manner for a number of years.[10–12] In the measurement process a focused laser beam is scanned across the surface of the semiconductor, and the current flowing in an external circuit between two nominally shorted remote ohmic contacts on either side of the scan area is measured, as shown in Fig. 1. The ohmic contacts are not required to be close to the laser position, and contacts to individual devices are not needed. Hence, only two contacts at remote positions on opposite edges of a wafer are needed to nondestructively characterize individual devices within large two-dimensional arrays of devices. This unique feature renders LBIC useful as an in-line process monitoring technique undertaken after junction formation but before flip-chip bonding to readout circuitry.

In both of the two main architectures used for planar HgCdTe P-on-n heterojunction photodiodes the N-n junction complicates the situation by providing additional built-in electric fields, and so from an LBIC point of view heterojunction photodiodes are much more complex to analyze than homojunctions. In this paper an efficient model for LBIC suitable for application to heterostructures is developed and used to examine the basic features of LBIC profiles obtained from various heterostructures. Experimental measurements are presented to support the simulations.

II. DEVICE PHYSICS AND MODELING

The formalism presented here follows a similar line to that of previous work aimed at homojunctions.[13–16] Firstly, the basic drift-diffusion model for heterostructures is presented and then cast in terms of quasi-Fermi potentials and a generalized potential. Then, under appropriate linearity of recombination mechanisms, a reduced model is developed which has significant computational advantages over the standard drift-diffusion model. The entire volume of the semiconductor to be modeled is denoted by Ω, and its boundary is denoted by Σ. In the steady-state case, the electron concentration n, hole concentration p, and electrostatic potential Ψ, are governed by the two steady-state conservation equations for electrons and holes:

$$\mathrm{div}\, J_e + q(G-U) = 0 \text{ with } J_e = qD_e \nabla n - q\mu_e n \nabla u, \quad (1)$$

$$-\mathrm{div}\, J_h + q(G-U) = 0 \text{ with } J_h = -qD_h \nabla p - q\mu_h p \nabla u. \quad (2)$$

Poisson's equation for the potential is given by

$$\nabla(\epsilon \nabla \Psi) = q(n-p-N), \quad (3)$$

where,

$$N = \begin{cases} N_D & \text{in the } n\text{-type region(s)}, \\ -N_A & \text{in the } p\text{-type region(s)}, \end{cases}$$

is the net doping profile of the sample, with $N_D > 0$ and $N_A > 0$ being the donor and acceptor impurity concentrations in the n- and p-type regions, respectively. On the portion of the boundary on which the remote ohmic contacts are placed, denoted by Σ_D, both thermal equilibrium and charge neutrality are assumed, which gives $np = n_i^2$ and $n-p=N$, respectively. This leads to the following Dirichlet boundary conditions on Σ_D:

$$n = n_0, \quad p = p_0, \quad \Psi = \Psi_0 = V_T \ln \frac{N + \sqrt{N^2 + 4n_i^2}}{2n_i} \quad (4)$$

where (n_0, p_0, Ψ_0) is the equilibrium state, and $V_T = kT/q$ is defined as the thermal voltage. Elsewhere on the boundary, denoted by Σ_N, Neumann boundary conditions are applicable. The simplest form is

$$\frac{\partial n}{\partial \boldsymbol{\nu}} = \frac{\partial p}{\partial \boldsymbol{\nu}} = \frac{\partial \Psi}{\partial \boldsymbol{\nu}} = 0, \quad (5)$$

where $\boldsymbol{\nu}$ is the unit vector in the outward normal direction, which represents electrically insulating boundaries. Alternatively, surface recombination can be included on part or all of Σ_N.[16]

In the above equations, G represents the generation of electron-hole pairs due to the incident illumination on the sample, and U is the recombination term. The absorption coefficient of the material and the illumination wavelength are responsible for the photogeneration profile which are embedded into the G term. The recombination is dependent on the various physical mechanisms at work within the semiconductor, which can further be expressed as

$$U = Q(np - n_i^2),$$

where the coefficient Q is often a function of carrier concentration and is determined by the particular recombination mechanism. The factor $np - n_i^2$ depends on the deviation from equilibrium and is common to all of the many recombination mechanisms, three of the most common being:

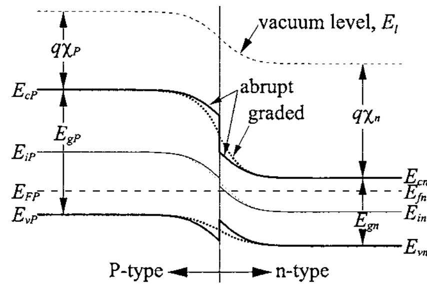

FIG. 2. Typical band diagram of a *P-n* heterojunction at thermal equilibrium showing the relationship between the vacuum level, E_l, electron affinities χ_P and χ_n, band gaps E_{gP} and E_{gn}, and the resulting conduction and valence bands. The case of an abrupt junction is shown with the solid lines, and the graded case is dotted. Note that there can be discontinuities in the conduction and valence bands when the junction is abrupt, possibly leading to spikes and/or wells in the generalized potential distribution.

$$\text{Shockley-Read-Hall model: } Q = \frac{1}{\tau_h(n+n_i) + \tau_e(p+n_i)},$$

$$\text{Auger model: } Q = C_e n + C_h p,$$

$$\text{Radiative model: } Q = B,$$

where C_e, C_h, and B are recombination parameters and, for simplicity, the trap energy in the Shockley-Read-Hall model has been chosen to be the midband-gap energy. This is a common assumption since this also happens to be the most efficient trap energy for trap assisted recombination and generation processes. In the modeling, Q can also be a weighted sum of contributions from each of the above models.

Using the same formalism of the previous authors,[17] a *generalized potential*, u, is defined as

$$-qu = \frac{1}{2}\left(E_c + E_v - kT\ln\frac{N_c}{N_v}\right).$$

Note that in the heterojunction case this is not the same as the electron potential because it is *not* the solution to Poisson's equation. However, it is related to the vacuum energy level, E_l, by band-structure parameters, and E_l is a solution to Poisson's equation. The relative positions of E_c and E_v with respect to the vacuum energy level are determined by the electron affinity, χ, and the band gap, E_g, of the material on either side of the junction, as shown in the band diagram of Fig. 2. These parameters can be related to the generalized potential as follows:

$$E_l = -q\Psi + \text{const.} = -qu + \frac{1}{2}\left(E_g + kT\ln\frac{N_c}{N_v}\right) + \chi.$$

The generalized potential is important because of its relationship to the electron and hole carrier concentrations via the electron and hole quasi-Fermi potentials v and w, respectively:

$$n = n_i \exp\left(\frac{E_f - E_i + qv}{qV_T}\right) = n_i \exp\left(\frac{u+v}{V_T}\right),$$

$$p = n_i \exp\left(\frac{E_i - E_f - qw}{qV_T}\right) = n_i \exp\left(\frac{-u-w}{V_T}\right).$$

In this regard the generalized potential is related to the energy difference between the Fermi level and the intrinsic energy level.

Assuming the Einstein relation holds, the equations for the new variables (v, w) and u become

$$\text{div}[n_i D_e e^{(u+v)/V_T}\nabla v] + G - n_i^2 Q(e^{v-w} - 1) = 0, \tag{6}$$

$$-\text{div}[n_i D_h e^{(-u-w)/V_T}\nabla w] + G - n_i^2 Q(e^{v-w} - 1) = 0, \tag{7}$$

$$\nabla\left[\epsilon\nabla\left(u - \frac{1}{q}\left\{\frac{1}{2}\left[E_g + kT\ln\left(\frac{N_c}{N_v}\right)\right] + \chi\right\}\right)\right] = q[n_i e^{(u+v)/V_T} - n_i e^{(-u-w)/V_T} - N]$$

with boundary conditions

$$\frac{\partial v}{\partial \boldsymbol{\nu}} = \frac{\partial w}{\partial \boldsymbol{\nu}} = \frac{\partial u}{\partial \boldsymbol{\nu}} = 0 \text{ on } \Sigma_N,$$

and

$$v = w = 0, \quad u = u_0 \text{ on } \Sigma_D.$$

In these equations u_0 is the equilibrium generalized potential, which is the solution of Poisson's equation with $v = w = 0$;

$$\nabla\left[\epsilon\nabla\left(u_0 - \frac{1}{q}\left\{\frac{1}{2}\left[E_g + kT\ln\left(\frac{N_c}{N_v}\right)\right] + \chi\right\}\right)\right] = q[n_i e^{u_0/V_T} - n_i e^{-u_0/V_T} - N]. \tag{8}$$

The photoinduced current flowing *out* of the semiconductor via one contact Σ_1 for each G is the LBIC signal and is given by

$$\begin{aligned} I_{\text{LBIC}}(G) &= \int_{\Sigma_1} (J_e + J_h)\cdot \boldsymbol{\nu} ds \\ &= q\int_{\Sigma_1}\left(D_e n\frac{\partial v}{\partial \boldsymbol{\nu}} + D_h p\frac{\partial w}{\partial \boldsymbol{\nu}}\right)ds \\ &= q\int_{\Sigma_1}\left[n_i D_e e^{(u+v)/V_T}\frac{\partial v}{\partial \boldsymbol{\nu}} + n_i D_h e^{(-u-w)/V_T}\frac{\partial w}{\partial \boldsymbol{\nu}}\right]ds. \end{aligned} \tag{9}$$

In general, all of the material parameters represented in the above set of equations are dependent on position, most noticeably across the heterointerface. Note that in the special case of homogeneous material, where the band structure is uniform across the material, the term $\{\frac{1}{2}[E_g + kT\ln(N_c/N_v)] + \chi\}$ and the intrinsic carrier concentration are both constant and so the equations simplify to those of the homojunction case outlined in Ref. 16.

Under low-level injection conditions $v, w \ll u_0$, and $v - w$ is small and so the system of Eqs. (6) and (7) can be linearized as follows:

$$\mathrm{div}(n_i D_e e^{u_0/V_T} \nabla v) - n_i^2 Q(v-w) = 0,$$

$$-\mathrm{div}(n_i D_h e^{-u_0/V_T} \nabla w) - n_i^2 Q(v-w) = 0,$$

and the boundary conditions remain unchanged. The linearized LBIC signal becomes

$$I_{\mathrm{LBIC}}(G) = q\int_{\Sigma_1}\left(n_i D_e e^{u_0/V_T}\frac{\partial v}{\partial \boldsymbol{\nu}} + n_i D_h e^{-u_0/V_T}\frac{\partial w}{\partial \boldsymbol{\nu}}\right)ds, \tag{10}$$

which is a surface integral over the contact Σ_1.

The reduced model

The reduced model is developed by introducing a new set of variables (ϕ,ψ) that is the solution to the following system of equations:[13–16]

$$\mathrm{div}(D_e n_i e^{u_0/V_T} \nabla \phi) - Q_0(\phi - \psi) = 0, \tag{11}$$

$$-\mathrm{div}(D_h n_i e^{-u_0/V_T} \nabla \psi) - Q_0(\phi - \psi) = 0, \tag{12}$$

where Q_0 is the recombination coefficient given by one or a combination of the following:

Shockley-Read-Hall model:

$$Q_0(u_0) = \frac{1}{\tau_h(e^{u_0/V_T}+1) + \tau_e(e^{-u_0/V_T}+1)},$$

Auger model: $Q_0(u_0) = n_i^2(C_e e^{u_0/V_T} + C_h e^{-u_0/V_T})$,

Radiative model: $Q_0 = n_i B$,

where C_e, C_h, and B are recombination parameters. The boundary conditions are

$$\frac{\partial \phi}{\partial \boldsymbol{\nu}} = \frac{\partial \psi}{\partial \boldsymbol{\nu}} = 0 \text{ on } \Sigma_N,$$

$$\phi = \psi = 1, \text{ on } \Sigma_1,$$

and

$$\phi = \psi = 0 \text{ on } \Sigma_2.$$

Note that the photogeneration term G no longer appears in Eqs. (11) and (12), and the boundary conditions for one of the contacts (Σ_1 in this case) have been modified. Using the divergence theorem, Eq. (10) becomes

$$I_{\mathrm{LBIC}}(G) = q\int_{\Omega} G(\psi - \phi)dx, \tag{13}$$

which is now a volume integral over the entire simulated region.[13–16] This version of the reduced model is valid in one, two or three dimensions and in any geometry, including arbitrarily shaped n- and/or p-type regions (including mesa-isolated devices), multiple n- and/or p-type regions (including arrays of devices) and arbitrary positioning of one or more heterointerfaces. In addition, the generation may be due to a focused laser, as is the case in this paper, or it may be due to any other uniform or nonuniform illumination of the semiconductor.

The difference $\psi-\phi$ [from Eq. (13)] represents the contribution to the LBIC signal for a delta function-shaped source of electron-hole pair photogeneration, at every possible position within the semiconductor; that is, the numerically obtained Greens function solution for the LBIC. In practical situations, when the photogeneration can be approximated by a delta function, such as when the illumination source is focused and the absorption coefficient is large, the LBIC profile would be given by a slice of the $\psi-\phi$ plot. That is, the front edge ($z=0$) for front-side illumination, or the back edge for back-side illumination. When the generation cannot be considered to be a delta function, an integration needs to be performed over the entire generation volume as represented by Eq. (13). This $\psi-\phi$ representation provides a powerful mechanism for considering the LBIC signal that would result from a wide variety of illumination sources.

The advantages of the reduced model stem from the fact that the differential equations for ϕ and ψ, given by Eqs. (11) and (12), are independent of the photogeneration term G. In particular, they only need to be solved once for a particular device structure, and then the LBIC signal for *any* laser configuration (position, low-level intensity, and wavelength) can be calculated by a simple integration using Eq. (13). In contrast, the full drift-diffusion model of Eqs. (1)–(5) requires a new solution for *every* different laser configuration. Hence, from a computational viewpoint the reduced model has the potential to be much simpler and faster than the full drift-diffusion model, which represents a significant advantage. Moreover, the representation $q(\psi-\phi)$ is actually an idealized LBIC image with *infinite* resolution in the sense that the laser beam profile is taken as the delta function $\delta(x_0,y_0,z_0)$ at any point within the semiconductor.

To summarize, the procedure for the derivation of the (ϕ,ψ) model consisted of three important steps. Firstly, low-level injection conditions were assumed so that the potential throughout the semiconductor could be approximated by the equilibrium potential and Poisson's equation could be decoupled. Secondly, the recombination terms in the drift-diffusion equations were linearized in terms of the difference between quasi-Fermi levels, $(v-w)$. And, finally, the system was transformed into the reduced model involving ϕ and ψ. It should be noted that the transformation into the reduced model is exact, and does not represent an additional approximation. Over the course of the derivation, the low-level injection condition and the linearization process have introduced approximations, and it is important to keep these in mind when considering the results of simulations. Other inaccuracies may be introduced through the use of the affinity rule for band offsets in the vacuum energy-level equation, which is only an approximation, and via the use of the Einstein relations when degenerate narrow band-gap semiconductors are considered. When these conditions are met, the induced current determined by using Eq. (13) will be an accurate representation of the induced current determined by the full drift-diffusion model.

III. SIMULATION OF HETEROJUNCTION PHOTODIODES

In this section the reduced model is used to examine the basic features of LBIC as applied to two contrasting *P*-on-*n* architectures. To simplify the simulations, only two-dimensional structures are considered and only devices in which the lateral dimensions are much greater than depletion widths. Additionally, the heterojunctions are assumed to be graded sufficiently that there are no spikes in the band structure, which allows the potential to be approximated by the piecewise constant scaled equilibrium potential in each of the individual regions. That is,

$$u = \ln\left[\frac{N}{2n_i} + \sqrt{\left(\frac{N}{2n_i}\right)^2 + 1}\right]$$

in each region, which means that $u > 0$ in all *n*-type regions and $u < 0$ in all *p*-type regions. A more thorough treatment should consider the situation in which the heterojunction may be abrupt and the band offset may be significant. This would introduce features such as potential barriers and two-dimensional electron gas populations, which would undoubtedly affect the LBIC signal.

In all simulations to follow the sample consists of a 9-μm-thick active layer of long-wavelength infrared $Hg_{0.78}Cd_{0.22}Te$ capped by a 1-μm-thick, wider band gap $Hg_{0.7}Cd_{0.3}Te$ layer, making the total epilayer thickness 10 μm. The total sample length is 800 μm, and the device region is 100 μm long and located in the center of the sample. The diffusion length in all regions is maintained at 20 μm, and it is assumed that there is no surface recombination. The LBIC magnitude is presented as a normalized value, indicating that the total photogenerated electron charge (and the total photogenerated hole charge) in Eq. (9) has been set to 1; that is, $q\int_\Omega G dx = 1$. As in the homojunction case, there are fundamental limits of ±0.5 to the normalized LBIC magnitude.[16]

One of the important observations of LBIC on heterojunctions is that in all cases the LBIC profile consists of a portion with the standard bipolar LBIC line scan, which is due to the *P*-*N* and *P*-*n* portions of the junction, combined with a second portion due to the *N*-*n* or N-n^+-n layers. The relative magnitudes of these two components depends on the specific material and geometrical parameters at the particular measurement temperature. There are four indicators that can be considered: (i) the magnitude of the induced current at the edge of the *P*-*N* junction (at the 350 and 450 μm positions in the simulations in this paper: see Fig. 1), (ii) the magnitude at the edge of the remote ohmic contact, (iii) the shape of the profile between the remote ohmic contact and the edge of the *P*-*N* junction, and (iv) the shape of the profile between the peaks of the standard bipolar LBIC at the 350 and 450 μm positions. Note that, as in the homojunction case, indicators (iii) and (iv) could be quantified using a form of the photocarrier spreading length in each of the two different layered structures.[18–20]

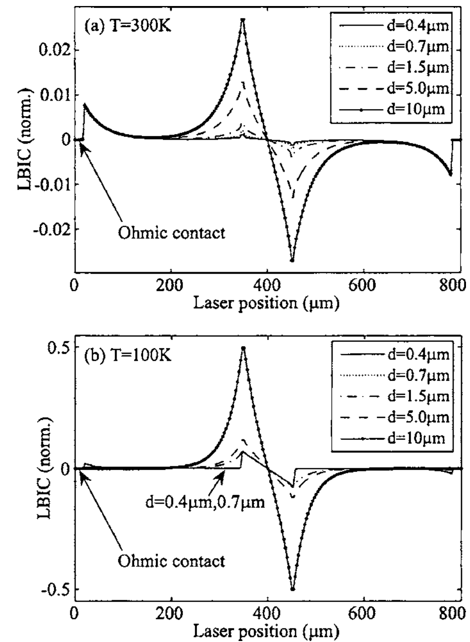

FIG. 3. The simulated dependence of LBIC on the *p*-type implanted junction depth, *d*, for the Rockwell architecture, at temperatures of (a) 300 K, and (b) 100 K, for photogeneration at the surface of the capping layer. The structures consist of a 9-μm active layer of $Hg_{0.78}Cd_{0.22}Te$ beneath a 1 μm capping layer of $Hg_{0.7}Cd_{0.3}Te$ with various depths of the *p*-type implanted junction.

A. The Rockwell architecture

General trends in the variation of the LBIC profile for the Rockwell architecture can be interpreted from the simulations presented in Figs. 3 and 4. Only the case of illumina-

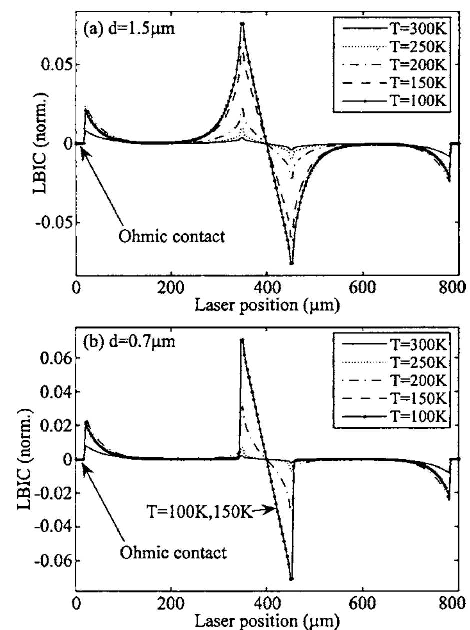

FIG. 4. The simulated temperature dependence of LBIC profiles of heterojunction photodiodes in the Rockwell architecture, with *p*-type implanted junction depths of (a) d=1.5 μm and (b) d=0.7 μm, to represent a properly formed device and a blind photodiode, respectively. The simulated structures consist of a 9-μm-thick active layer of $Hg_{0.78}Cd_{0.22}Te$ beneath a 1 μm capping layer of $Hg_{0.7}Cd_{0.3}Te$ at various temperatures, and the photogeneration is confined to the surface of the capping layer.

tion with sufficiently short wavelength, and hence very shallow photogeneration at the surface of the wide band-gap capping layer, is presented. This particular situation has been chosen as a representative case rather than attempting to present simulations of all possibilities, and also because it is similar to the measurement configuration used in Sec. IV. As is explained later in this section, there are many contrasting possibilities regarding the case of photogeneration using a focused laser in heterostructures which, in particular, are dependent on the illumination wavelength.

Figures 3 and 4 indicate that the current induced when the laser is at the junction edges at the 350 and 450 μm positions increases as the temperature is reduced, and also increases as the depth of the implanted *p*-type material increases. This is the same behavior as occurs for a homojunction photodiode.[21] Figure 4 indicates that the magnitude of the current induced when the laser is adjacent to the remote ohmic contact appears to increase and then decrease slightly as the temperature is reduced from 300 towards 100 K, with a magnitude that peaks at around 200 K. However, the results shown in Fig. 3 suggest that the dependence on depth of this part of the profile is less distinguishable and requires further examination. Furthermore, there is little variation in the effective photocarrier-spreading length dictating the shape of the profile between the remote contact and the edge of the device, as is evident from the shape of the curves in Figs. 4(a) and 4(b).

As mentioned previously, one of the critical issues with the Rockwell architecture is the depth of the implanted *p*-type region, with incorrectly formed devices resulting if the depth is too shallow or too deep. Figures 3 and 4 indicate that for short wavelength illumination, there are no trends in the variation in LBIC profiles that would prove useful and reliable for the identification of incorrectly formed devices. In all of the simulations presented thus far, the photogeneration of electron-hole pairs has been assumed to occur exclusively at the surface of the capping layer. However, in contrast with the homojunction case, in which the photogeneration of electron-hole pairs will always be greatest at the illuminated surface, the heterojunction case allows a few more possibilities for the physical location of the photogeneration volume. Potentially, this allows for more precise and useful information about the depth of the implanted *p*-type region to be obtained.

When the energy of the incident illumination is greater than the band gap of the capping layer, most of the photogeneration of electron-hole pairs occurs close to the surface of this layer. Alternatively, when the wavelength of the illumination is chosen such that its energy is less than the band gap of the capping layer, but greater than the bandgap of the active layer, the photogeneration will be most significant in the active layer. Hence, with judicious choice of illumination wavelengths it is possible to selectively probe the two different layers independently.

The $\psi-\phi$ representation for two different cases of the Rockwell architecture is presented in Fig. 5. The configurations are similar to those studied in Figs. 3 and 4, with a 9-μm-thick active layer of $Hg_{0.78}Cd_{0.22}Te$ beneath a 1 μm capping layer of $Hg_{0.7}Cd_{0.3}Te$; however, the lateral dimensions have been made smaller to allow better viewing. It is clear from Fig. 5(a), that there will only be minor differences in the LBIC profile obtained when the active layer and the capping layer are individually excited. Slices through the $\psi-\phi$ map at the surface ($z=0$, where z is the coordinate of depth from the surface of the structure) and at the top of the active layer ($z=1$) are very similar. Hence, when the implanted *p*-type region extends deeper than the heterointerface, and a proper photodiode is formed having the same cutoff wavelength as the active layer, selective excitation will not provide any assistance in determining the actual depth of the implanted region. However, when the implanted junction depth does not reach the active layer, as is the case portrayed by Fig. 5(b), the $\psi-\phi$ representation when photogeneration occurs at the surface ($z=0$) is significantly different from when it occurs at the top of the active layer ($z=1$). Hence, in this case, individual excitation of the two layers will produce significantly different LBIC profiles. However, this effect is less pronounced at high temperatures and so low temperatures would need to be used in order to enhance the junction depth monitoring process.

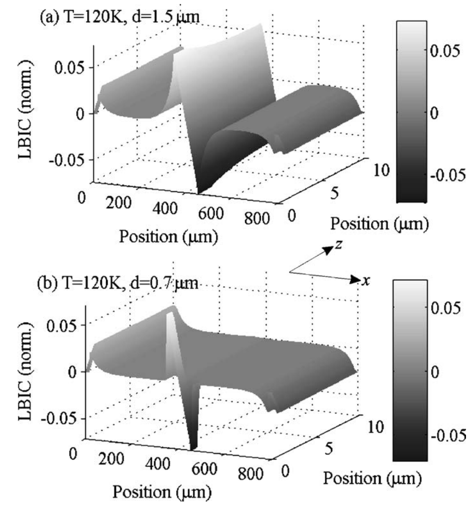

FIG. 5. The $\psi-\phi$ representation of LBIC applied to Rockwell architecture heterojunction photodiodes at 120 K. The simulated structures consist of a 9-μm active layer of $Hg_{0.78}Cd_{0.22}Te$ beneath a 1 μm capping layer of $Hg_{0.7}Cd_{0.3}Te$. Recall that this representation depicts the contribution to the LBIC signal that would occur from photogeneration at any position within the semiconductor. The *p*-type implanted depth is (a) $d=1.5$ μm and (b) $d=0.7$ μm, to represent a properly formed device and a blind photodiode, respectively.

From the above discussion, it seems plausible that selective excitation of the individual layers within the heterostructure could be used to determine whether or not the *p*-type implanted region has reached the active layer. However, this is only a partial solution to the problem, since the optimal placement of this junction is within the active layer but close to the heterointerface. Without further study, it seems a very difficult task to accurately determine the depth of the *p*-type-implanted region once it is known to lie within the narrow band-gap active layer.

B. The architecture of Bahir *et al.*

Figures 6 and 7 present simulation results showing the LBIC profile for the Bahir architecture with variations in

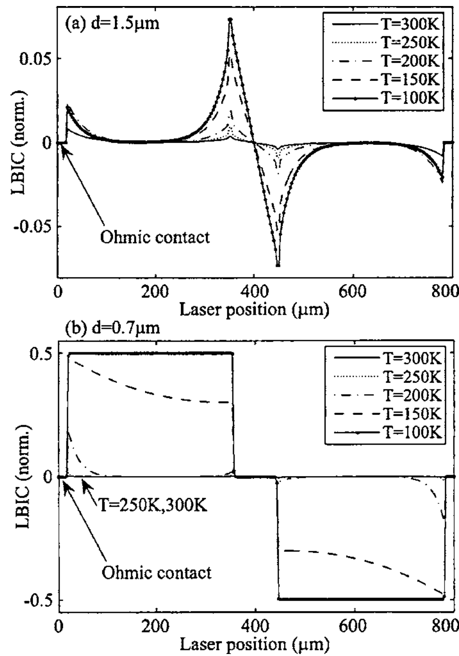

FIG. 6. The simulated temperature dependence of LBIC profiles of heterojunction photodiodes in the architecture of Bahir *et al.*, with isolating junction depths of (a) $d=1.5$ μm and (b) $d=0.7$ μm, to represent a properly formed device and an incompletely isolated photodiode, respectively. The simulated structures consist of a 9-μm active layer of $Hg_{0.78}Cd_{0.22}Te$ beneath a 1 μm capping layer of $Hg_{0.7}Cd_{0.3}Te$ at various temperatures, and the photogeneration is confined to the surface of the capping layer.

both the temperature and depth of the isolating n-type doping. Once again, only the case of illumination with a sufficiently short wavelength, and hence very shallow photogeneration at the surface of the wide band gap capping layer, is presented.

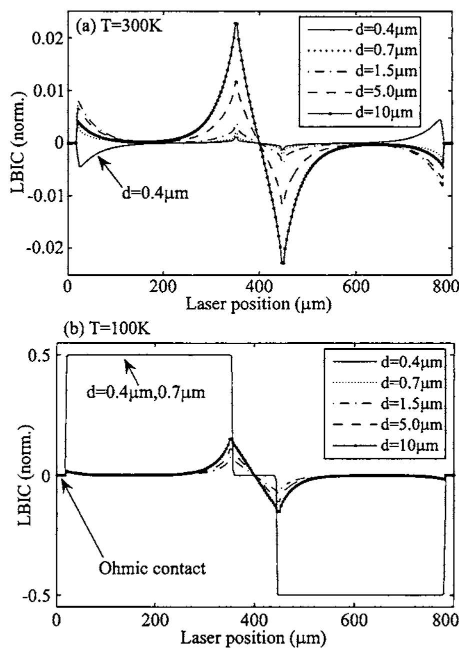

FIG. 7. The simulated dependence of LBIC on the isolating junction depth, d, for the architecture of Bahir *et al.*, at temperatures of (a) 300 K, and (b) 100 K, for photogeneration at the surface of the capping layer. The simulated structures consist of a 9-μm-thick active layer of $Hg_{0.78}Cd_{0.22}Te$ beneath a 1 μm capping layer of $Hg_{0.7}Cd_{0.3}Te$ with various depths of the isolating n-type dopant.

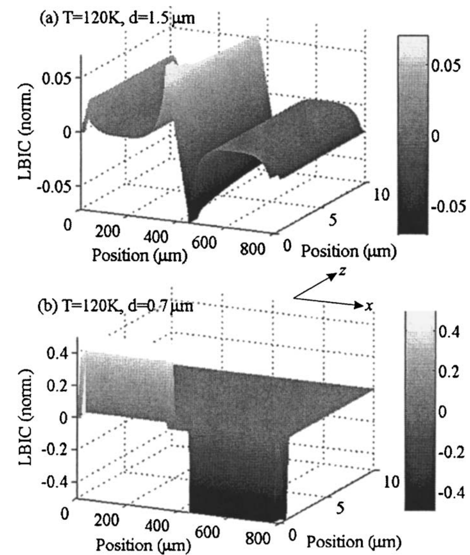

FIG. 8. The $\psi-\phi$ representation of LBIC applied to heterojunction photodiodes in the Bahir architecture. The simulated structures consist of a 9-μm active layer of $Hg_{0.78}Cd_{0.22}Te$ beneath a 1 μm capping layer of $Hg_{0.7}Cd_{0.3}Te$ at 120 K. This representation depicts the contribution to the LBIC signal that would occur from photogeneration at any position within the semiconductor. The p-type-implanted depth is (a) $d=1.5$ μm and (b) $d=0.7$ μm, to represent a properly formed device and an incompletely isolated photodiode, respectively.

Whilst the temperature dependence for the ideal device structure, depicted in Fig. 6(a), shows similar trends to the Rockwell case [see Fig. 4(a)], there are significant anomalies in the temperature dependence for this configuration when the isolation doping does not reach the active layer, as depicted in Fig. 6(b). As the temperature is reduced, the magnitude of the LBIC signal when the laser is incident on the *N-P-n* triple-layered structure increases dramatically, and saturates at the theoretical maximum normalized value of ± 0.5.[16] Under these circumstances, all of the photocurrent collected by the junction flows via the external circuit as the LBIC signal.

Figure 7 shows the dependence of the line profile on the depth of the isolating donor doping for temperatures of 300 and 100 K. Clearly, the lower-temperature profile for the incorrectly formed devices (that is, when the isolating doping is at a depth of less than 1 μm and does not reach the heterojunction) is again significantly larger than for the deeper junctions which form proper isolated photodiode structures. Hence, these results indicate that it should be relatively straightforward to identify incorrectly formed devices using a single LBIC profile obtained with a sufficiently short wavelength, with low temperatures enhancing the identification process. Another interesting feature worthy of note is that the signal from the layered structure (when the laser is adjacent to the remote ohmic contacts) can be of opposite polarity to that of the device itself, as shown in the curve representing an implant depth of 0.4 μm in Fig. 7(a).

As described in the previous section, an appropriate choice of illumination wavelengths allows the possibility of selectively exciting the two different device layers individually. The $\psi-\phi$ representation for two different depths of the isolating junction depth is presented in Fig. 8, with a prop-

erly formed device in Fig. 8(a) and an incorrectly formed device in Fig. 8(b). It should be possible to confirm the identification of incorrectly formed devices of the Bahir architecture by comparison of LBIC profiles obtained at low temperatures using two judiciously chosen illumination wavelengths. The short wavelength illumination, corresponding to photogeneration at the surface of the wide band gap capping layer [$z=0$ in Fig. 8(b)], produces an LBIC profile significantly different to that obtained with longer wavelength illumination that has been selected to generate photocarriers at the upper interface of the narrow bandgap active region ($z=1$). This is not the case for properly formed devices, as portrayed in Fig. 8(a).

IV. EXPERIMENTAL RESULTS

To further examine the application of LBIC to heterojunctions, a series of devices was fabricated based on the Bahir architecture. The starting *P*-on-*n* heterojunction material was grown via liquid-phase epitaxy (LPE) by Fermionics corporation and designated as wafer #31105. By nature, the LPE process is a high-temperature growth regime and, hence, is more likely to result in a grading of the heterojunction than molecular beam epitaxy (MBE) growth processes, closer matching the assumptions under which the reduced model of Sec. II was developed. In addition, the situation may be further complicated by a slightly different depth of the heterojunction and metallurgical junction, erring to a possible *P*-*p*-*n* as-grown structure. Data from Fermionics suggests that the as-grown material consisted of a 15-μm-thick active layer of midwavelength infrared $Hg_{0.68}Cd_{0.32}Te$ with *n*-type doping of $N_D=3\times10^{15}$ cm^{-3}, with a 2 μm capping layer of wider band-gap material with mole ratio approximately 0.37 and *P*-type doping of $\sim4\times10^{16}$ cm^{-3}. The electron mobility of the active layer was quoted as $\mu_e=2\times10^4$ cm^2 V^{-1} s^{-1} at 80 K. A reactive ion etching (RIE) plasma-type conversion process[22] was used for the isolation procedure with two different RIE durations (2 and 12 min) on different parts of the same sample. The measurements were performed at a temperature of $\sim$140 K using a 1.047 -μm wavelength diode-pumped Nd:YLF (yttrium lithium fluoride) laser. Illumination at this wavelength is expected to generate electron-hole pairs within the first 1 μm of the capping layer.

Results from the measurements at $\sim$140 K are displayed in Figs. 9 and 10, which show sample LBIC maps and line profiles, respectively. The line profiles shown in Fig. 10 were extracted from cross-sections taken through devices with side dimension of 400 μm, as shown in the lower half of each of the LBIC maps of Fig. 9. Clearly, there is a significant difference between the two cases. The comparison of these measured LBIC profiles with the simulations of Figs. 6 and 7 suggests that the type conversion resulting from the 12-min duration RIE definitely reaches the heterointerface and so proper *P*-on-*n* devices are formed. In contrast, it is evident that the 2-min RIE-type conversion process does not result in properly isolated *P*-*n* heterojunction diodes.

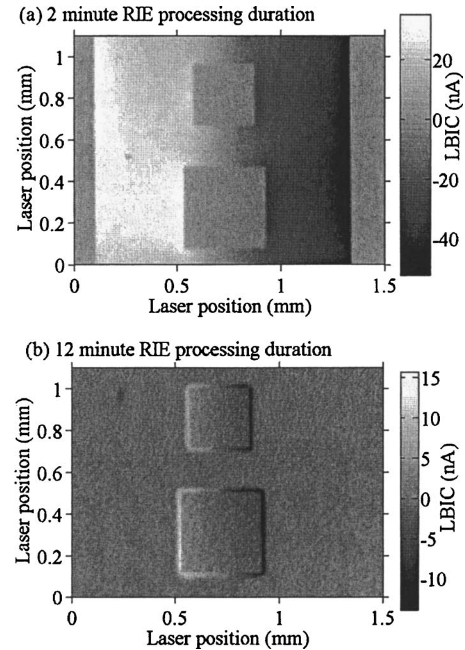

FIG. 9. LBIC maps measured at $\sim$140 K on Bahir architecture heterojunction photodiode structures fabricated via (a) 2-min and (b) 12-min RIE processing duration on wafer #31105.

V. SUMMARY AND CONCLUSIONS

In the presence of heterostructures, analysis of LBIC maps and line profiles is extremely complicated due to the many heterojunctions and metallurgical junctions that contrive to influence the LBIC signal. A reduced model has been developed that has significant advantages over the full drift-diffusion model for the calculation of LBIC signals. Use of the reduced model and the associated $\psi-\phi$ representation of the particular device structure allows the LBIC profiles for a wide range of illumination conditions to be considered in a unified manner. The $\psi-\phi$ representation depicts the contribution to the LBIC signal that would occur from photogeneration at any position within the semiconductor, and is particularly useful for heterostructures where judicious choice of illumination wavelength can result in photogeneration within the different layers of the device structure.

The reduced model was used to examine the basic fea-

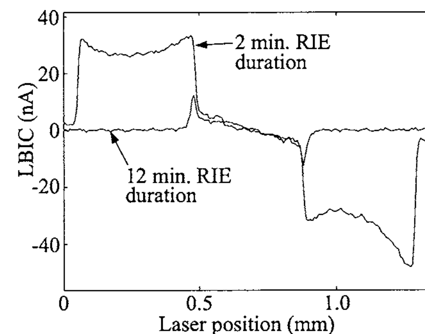

FIG. 10. LBIC profiles measured at $\sim$140 K on Bahir architecture heterojunction photodiode structures fabricated via 2- and 12-min RIE processing duration on wafer #31105. These line profiles were obtained from cross sections taken through the 400-μm devices shown in the lower half of the LBIC maps of Fig. 9.

tures of LBIC as applied to two types of planar *P*-*n* HgCdTe heterojunction photodiodes. In particular, the question of identifying poorly formed devices during the fabrication process was addressed. It has been shown that incorrectly formed devices of the Bahir architecture are easily identifiable with a single (short) illumination wavelength if measurements are performed at sufficiently low temperatures. On the other hand, identification of incorrectly formed devices for the Rockwell architecture relies on comparison of LBIC profiles obtained using two different wavelengths of laser illumination.

There are a number of areas that still require further work for a more complete understanding of LBIC in heterojunction devices to be developed. In terms of development, the reduced model could be modified to include the effects of abrupt junctions and band offsets, which requires solution of Poisson's equation [Eq. (8)] as well as the inclusion of thermionic emission and/or tunneling mechanisms. This would facilitate the simulation of a wider variety of heterostructures which incorporate spikes and depressions in the band structure, and that can lead to such features as two-dimensional electron gases. In addition, further analytic modeling of the various layered structures making up parts of devices is warranted, possibly including thermionic emission and/or tunneling mechanisms to account for carrier injection across potential spikes. For example, considering the Bahir architecture portrayed in Fig. 1(b) and discussed in the latter part of Sec. III, the devices consist of *P*-on-*n* layers combined with either N-n^+-n or *N*-*P*-*n* triple-layered structures between devices, depending on the depth of the isolating donor doping. Such layered structures can give rise to effective photocarrier spreading lengths for the *n*-on-*p* homojunction layers. It is known that there are several different possibilities that the potential distribution can take, and the resulting dipole between the two ends of a particular layered structure can even change polarity with different temperature, as has been illustrated in Fig. 7(a). Such effects can only be utilized as characterization tools if further work is able to provide a more complete physical model.

ACKNOWLEDGMENTS

The authors wish to thank the Australian Research Council for their financial support of this work. Additionally, one of the authors (D.A.R.) wishes to thank the Australia-Israel Scientific Exchange Foundation (AISEF) for the provision of an AISEF Postgraduate Fellowship to undertake part of this work at The Technion-Israel Institute of Technology, Israel.

[1] J. Wenus, J. Rutkowski, and A. Rogalski, IEEE Trans. Electron Devices **48**, 1326 (2001).
[2] S. Terterian, M. Chu, S. Mesropian, H. Gurgenian, J. D. Benson, and J. H. Dinan, J. Electron. Mater. **33**, 615 (2004).
[3] J. M. Arias, J. G. Pasko, M. Zandian, S. H. Shin, G. M. Williams, L. O. Bubulac, R. E. DeWames, and W. E. Tennant, J. Electron. Mater. **22**, 1049 (1993).
[4] J. M. Arias, J. G. Pasko, M. Zandian, S. H. Shin, G. M. Williams, L. O. Bubulac, R. E. DeWames, and W. E. Tennant, Appl. Phys. Lett. **62**, 976 (1993).
[5] A. I. D'Souza, L. C. Dawson, E. J. Anderson, and A. J. Markum, J. Electron. Mater. **26**, 656 (1997).
[6] G. Bahir, in *Physics of Semiconductor Devices*, edited by V. Kumar and S. K. Agarwal (Narosa, New Delhi, 1998), pp. 697–704.
[7] G. Bahir, V. Garber, and A. Dust, J. Electron. Mater. **30**, 704 (2001).
[8] C. A. Musca, J. Antoszewski, J. M. Dell, L. Faraone, and S. Tertarian, J. Electron. Mater. **32**, 622 (2003).
[9] M. Chu, S. Mesropian, S. Terterian, H. K. Gurgenian, and M. Pauli, J. Electron. Mater. **33**, 609 (2004).
[10] J. Bajaj, L. O. Bubulac, P. R. Newman, W. E. Tennant, and P. M. Raccah, J. Vac. Sci. Technol. A **5**, 3186 (1987).
[11] J. Bajaj, W. E. Tennant, and P. R. Newman, J. Vac. Sci. Technol. A **6**, 2757 (1988).
[12] J. Bajaj, W. E. Tennant, R. Zucca, and S. J. C. Irvine, Semicond. Sci. Technol. **8**, 872 (1993).
[13] S. Busenberg, W. Fang, and K. Ito, SIAM J. Appl. Math. **53**, 187 (1993).
[14] W. Fang and K. Ito, SIAM J. Appl. Math. **52**, 1611 (1992).
[15] W. Fang and K. Ito, SIAM J. Appl. Math. **54**, 1067 (1994).
[16] W. Fang, K. Ito, and D. A. Redfern, SIAM J. Appl. Math. **62**, 2149 (2002).
[17] Z. Yu and R. W. Dutton, *SEDAN III-A generalized electronic material device analysis program*, Stanford, California 94305, July 1985.
[18] G. Lucovsky, J. Appl. Phys. **31**, 1088 (1960).
[19] J. Degani, D. P. Wilt, and P. Besomi, J. Appl. Phys. **56**, 468 (1984).
[20] D. A. Redfern, C. A. Musca, J. M. Dell, and L. Faraone, J. Electron. Mater. **33**, 560 (2004).
[21] D. A. Redfern, W. Fang, K. Ito, C. A. Musca, J. M. Dell, and L. Faraone, Solid-State Electron. **48**, 409 (2003).
[22] J. M. Dell, J. Antoszewski, M. H. Rais, C. A. Musca, J. K. White, B. D. Nener, and L. Faraone, J. Electron. Mater. **29**, 841 (2000).